minerals

MDPI

Article

Formation of Authigenic Low-Magnesium Calcite from Sites SS296 and GC53 of the Gulf of Mexico

Huiwen Huang [1,2,†], Shanggui Gong [3,†], Niu Li [1,3], Daniel Birgel [4], Jörn Peckmann [4], Meng Jin [1,2], Ming Cheng [1], Harry H. Roberts [5], Duofu Chen [3,6] and Dong Feng [1,3,6,*]

1 CAS Key Laboratory of Ocean and Marginal Sea Geology, South China Sea Institute of Oceanology, Chinese Academy of Sciences, Guangzhou 510301, China; huiwenhuang@scsio.ac.cn (H.H.); liniu@scsio.ac.cn (N.L.); jinmeng@scsio.ac.cn (M.J.); chengming@scsio.ac.cn (M.C.)
2 University of Chinese Academy of Sciences, Beijing 100049, China
3 Shanghai Engineering Research Center of Hadal Science and Technology, College of Marine Sciences, Shanghai Ocean University, Shanghai 201306, China; gsg@scsio.ac.cn (S.G.); dfchen@shou.edu.cn (D.C.)
4 Institute for Geology, Center for Earth System Research and Sustainability, Universität Hamburg, 20146 Hamburg, Germany; daniel.birgel@uni-hamburg.de (D.B.); joern.peckmann@uni-hamburg.de (J.P.)
5 Coastal Studies Institute, College of the Coastal and Environment, Louisiana State University, Baton Rouge, LA 70803, USA; hrober3@lsu.edu
6 Laboratory for Marine Mineral Resources, Qingdao National Laboratory for Marine Science and Technology, Qingdao 266061, China
* Correspondence: feng@scsio.ac.cn; Tel.:+86-20-89022336
† These authors contributed equally to this work.

Received: 30 March 2019; Accepted: 23 April 2019; Published: 25 April 2019

Abstract: Authigenic low-magnesium calcite (LMC)—a mineral phase that should precipitate in calcite seas rather than today's aragonite sea—was recently discovered at the seafloor of the Gulf of Mexico (GoM) at water depths of 65 m (site SS296) and 189 m (site GC53). This study investigates the mineralogical, petrographic, and geochemical characteristics of LMC from both sites to reveal its formation process. The $\delta^{18}O$ values of LMC from site SS296 cluster in two groups (−0.6‰ to 1.7‰; 6.3‰ to 7.5‰) and the presence of cone-in-cone texture in the samples with lower $\delta^{18}O$ values suggest precipitation at higher temperatures and greater depth. Low $\delta^{18}O$ values of LMC from site GC53 ranging from −9.4‰ to −2.5‰ indicate an influence of meteoric waters during formation. LMC at both sites reveals a wide range of $\delta^{13}C$ values (−17.4‰ to 2.6‰), indicating various carbon sources including seawater and/or organic matter. This interpretation is further supported by the $\delta^{13}C$ values of organic carbon extracted from the LMC lithologies ($\delta^{13}C_{org}$: from −26.8‰ to −18.9‰). Relatively low Sr concentrations of LMC samples regardless of variable $^{87}Sr/^{86}Sr$ ratios, ranging from 0.707900 to 0.708498 for site GC53 and from 0.709537 to 0.710537 for site SS396, suggest the exchange of Sr between pore fluids and ambient sediments/rocks. The observed wide range of $^{87}Sr/^{86}Sr$ ratios and the enrichment of Fe and Mn in LMC is in accordance with pore fluids deriving from the dissolution of Louann salt. Overall, this study reveals that the formation of LMC at sites SS296 and GC53 was favored by the presence of low Mg/Ca ratio pore fluids resulting from salt dissolution in subsurface environments when sufficient dissolved inorganic carbon was available. These results are essential for understanding the formation of marine LMC at times of an aragonite sea, highlighting the role of formation environments—open environments close to or at the seafloor vs. confined subseafloor environments typified by pore waters with a composition largely different from that of seawater.

Keywords: low-magnesium calcite; aragonite sea; carbonates; salt diapirs; Gulf of Mexico

1. Introduction

The oscillations of aragonite seas and calcite seas since the beginning of the Paleozoic Era are reflected in the dominant mineralogies of primary carbonate minerals in marine environments [1–3]. Such recurrent change is induced by oscillation in the Mg/Ca ratio (referring to the Mg/Ca mole ratio here) of Phanerozoic seawater [1,2]. Low-magnesium calcite (LMC: <5 mol % $MgCO_3$ [4]) predominantly precipitates as stable carbonate mineral during times of a calcite sea [3]. The occurrence of primary LMC is, therefore, a good indicator of a low Mg/Ca ratio (<2) of seawater [3]. In today's aragonite sea (an Mg/Ca ratio of seawater ~5.2; [1]), most carbonate minerals are either high-Mg calcite (HMC) or aragonite (e.g., [5,6]). Interestingly, the occurrence of LMC dominated non-skeletal carbonates was reported for some marine settings, such as Monterey Bay [7] and the Gulf of Mexico (GoM) [5,8,9]. LMC from Monterey Bay with negative $\delta^{18}O$ values ranging from −5.8‰ to −5.4‰ and $\delta^{13}C$ values of approximately −11.0‰ most likely formed under the influence of locally present meteoric water, reflecting either primary precipitates or products of the recrystallization of seep carbonates under meteoric conditions [7]. LMC from site AC601 at a water depth of 2340 m in the GoM has been suggested to result from brine fluid flow associated with hydrocarbon seepage [5]. These brines are relatively Ca^{2+}-enriched and Mg^{2+}-depleted (an Mg/Ca ratio < 0.7) relative to modern seawater [5,10]. Moreover, the occurrence of marine LMC was also reported as a minor component of carbonate lithologies from many seafloor environments, such as the South China Sea and Cascadia margin (e.g., [11,12]).

Given the metastability of aragonite and HMC, both minerals tend to convert into more stable calcite [13]. Thus, primary LMC is potentially an excellent archive of paleoenvironmental conditions in the geologic record [14]. However, petrographic features and geochemical signatures need to be used beforehand to test if LMC is of primary origin [15,16]. Carbon, oxygen, and strontium isotopes and elemental compositions have been used to reconstruct the diagenetic environment and processes that triggered LMC formation [7–9,12].

Here, we report the discovery of carbonates dominated by LMC from site SS296 at a water depth of 65 m and site GC53 at a water depth of 189 m in the GoM. We evaluate whether LMC is of primary origin, constrain fluid sources, and reconstruct the formation processes through a combination of petrographic and geochemical analyses. For comparison, two samples that are mainly composed of HMC and aragonite from site GC53 were investigated along with the LMC dominated lithologies.

2. Geological Setting and Sampling

The GoM began forming during the Triassic to Early Cretaceous, rifting between the Yucatan microplate and the North American plate [17]. The rifting resulted in stretching of continental crust that opened up a small connection with the Atlantic Ocean, leading to suitable conditions for Louann salt deposition. The Louann salt ceased to deposit after the basin opening. Subsequently, the margin of the GoM received input of abundant terrigenous sediments, resulting in thick sedimentary strata overlying the Louann salt [18,19]. Driven by rapid, yet patchy deposition of terrigenous sediment, widespread salt diapirism coupled with a series of fractures developed in subsurface sediments onshore and offshore the Gulf region [20]. It has been discovered that seawater, groundwater, and hypersaline seawater were enclosed in continental shelf sediments [21–24], which could migrate along fractures and interact with ambient sediments, resulting in complex pore water geochemistry.

Salt dome cap rocks resulting from salt dissolution, element substitution, and sulfate reduction were widely discovered at the top of salt diapirs in the GoM [20,25]. As salt diapirs dissolve, less soluble anhydrite and gypsum accumulate at the margin of salt structures [25]. Barite and celestine tend to form as calcium in anhydrite and gypsum is replaced by barium or strontium [25]. In case of the supply of sufficient hydrocarbons, microbial sulfate reduction coupled with hydrocarbon degradation results in precipitation of calcite, native sulfur, and sometimes metal sulfide in salt domes [20,25].

Carbonates studied herein were sampled by the *Pisces II* (Dive 88-22 and 89-1) and *Johnson Sea-Link* (JSL Dive 3110 and 3112) research submersibles at the seafloor of sites SS296 and GC53. Salt diapirs

occur in the buried sediments at both sites [26,27]. Site SS296 is located on the inner continental shelf. It is situated about 7 km northwest of Ship Shoal Block 318, which includes a salt withdrawal basin with a maximum depth of 7300–7800 m [28]. To the north, east, and west, the salt withdrawal basin is bounded by generally continuous salt ridges, which locally rise to about a 2000 m depth below sea level [28]. Site GC53 is located at the edge of the continental shelf (Figure 1). The salt diapir at site GC53 is near a structural trap, containing crude oil [29]. Faults, gas seeps, brine seeps, and mud volcanoes have been reported from the surroundings of GC53 [30]. Locally occurring abundant authigenic carbonates and *Beggiatoa* mats were attributed to hydrocarbon seepage [31].

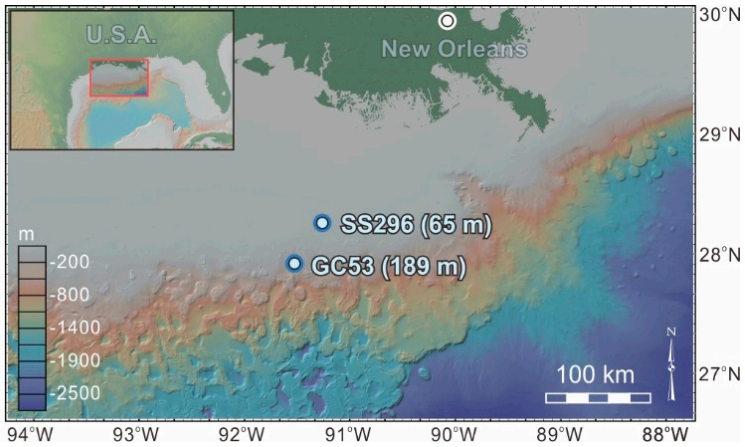

Figure 1. Locations of sites SS296 and GC53 in the Northern Gulf of Mexico. Maps were created using GeoMapApp software.

3. Methods

3.1. Mineralogy and Petrography

Petrographic observations using thin sections were conducted with a LEICA-DMRX optical microscope with Leica Qwin software (Version V2.6, Leica Microsystems Imaging Solutions Ltd., Cambridge, UK). Additionally, the microfabric of carbonates was examined on freshly broken surfaces using a Quanta 400 Scanning Electron Microscope (SEM) operating at 10–20 kV at Guangzhou Institute of Energy Conversion, Chinese Academy of Sciences (CAS) (Guangzhou, China). The samples were coated with gold to a thickness of 20 nm.

Samples for the identification of mineralogies and the determination of relative concentrations of carbonate minerals were crushed into a powder (<200 mesh) using an agate mortar and pestle. Mineralogy was determined using X-ray diffraction (XRD) with a Rigaku DXR 3000 computer-automated diffractometer at the Guangzhou Institute of Geochemistry, CAS. The X-ray source was a Cu anode operated at 40 kV and 40 mA using CuKα radiation equipped with a diffracted beam graphite monochromator. Orientated samples were scanned at an interval of 5–65° (2θ) with a step size of 0.02° and a count time of 5 s per step. Diverging, scattering, and receiving slits were 0.5°, 0.5°, and 0.15 mm, respectively. The $MgCO_3$ content of carbonate minerals was determined by the position of the (104) peak [32].

3.2. Major and Trace Element Analyses

The powdered samples were divided into two parts, which were analyzed for major element concentrations of bulk samples and trace element concentrations of carbonate phases, respectively. For major element analysis of bulk samples, samples were dissolved in HF–HNO_3 solutions. For trace element analysis of carbonate phases, samples were dissolved in 5% acetic acid solutions. Preparation of samples followed the methods of Hu et al. [8]. Afterwards, major elements were measured using a Varian Vista Pro ICP-AES and trace elements were measured using a Perkin-Elmer Sciex

ELAN 6000 ICP-MS at the Institute of Geochemistry, CAS. Accuracy was determined using several reference standards (GSR-3, GSD-4, GSD-6, OU-6, and GSR-12 for a major element test; OU-6, AMH-1, and GBPG-1 for the trace element test) and is better than 5%. Rare earth element (REE) patterns of authigenic carbonates were normalized against Post Archean Australian Shale [33].

3.3. Isotope Analyses

Subsamples were micro-drilled from the surface of polished slabs for oxygen, carbon, and strontium isotope analysis. Carbon and oxygen stable isotope compositions of carbonates were measured using a GV Isoprene II stable isotopic mass spectrometer at the Guangzhou Institute of Geochemistry, CAS and Louisiana State University (LSU) (Baton Rouge, LA, USA). Samples were reacted with 100% phosphoric acid at 90 °C and the generated CO_2 was extracted and purified before the measurement. Results are reported relative to the Vienna Pee Dee Belemnite (VPDB) standard, and the precision is on the order of 0.1‰ (2σ) for both $\delta^{13}C$ and $\delta^{18}O$ values. $^{87}Sr/^{86}Sr$ ratios were determined using a Triton thermal ionization mass spectrometer at the Guangzhou Institute of Geochemistry, CAS. Samples were dissolved in 1 mol/L ultra-pure acetic acid. The solutions were centrifuged, and the decantate was evaporated dry. Samples were then dissolved in 5 mol/L HNO_3 and loaded onto columns containing Eichrom Sr-specific resin. $^{87}Sr/^{86}Sr$ ratios are reported relative to an $^{87}Sr/^{86}Sr$ ratio of 0.71025 for SRM-987, of which replicate analyses indicate uncertainties of ±0.000011 (1σ).

To extract organic matter, about 5 g of carbonate powders were dissolved by slowly adding 1 mol/L HCl until the reaction ceased (no more bubbles produced). The residue was washed with distilled water and oven-dried overnight at <50 °C. The carbon content, nitrogen content, and $\delta^{13}C_{org}$ values of the residue were determined by an Elemental Analyzer (EA) at 980 °C and a Thermo Electron Delta V Plus Advantage mass spectrometer in a continuous-flow mode at LSU. The $\delta^{13}C_{org}$ values are reported relative to the VPDB standard. Precision is on the order of 0.1‰ (2σ) for $\delta^{13}C_{org}$ values, on the order of 0.1% (2σ) for carbon concentrations, and 0.3% (2σ) for nitrogen concentrations. The organic carbon and nitrogen concentrations of bulk samples were obtained by relating carbon and nitrogen concentrations of the residual powder and to the mass ratios of powder prior to and after decalcification.

4. Results

4.1. Samples, Mineralogy, and Petrographic Features

The carbonates are dense, homogenous micritic lithologies except for samples 3112R1 and 3112R3, which show an irregular texture and stratification, respectively (Figure 2). The dense carbonates contain few bioclasts and are mainly composed of microcrystalline crystals, which consist of cement quartz and other terrigenous minerals (Table 1; Figures 3 and 4). The dense lithologies are dominated by LMC according to XRD analysis (Figure S1). Some LMC crystals are of nm scale (Figure 4C) and are intermingled between clayey materials (Figure 4D). Siderite occurs in several of the dense carbonates and pyrite was recognized in thin section (Table 1; Figure 3C,D). Additionally, cone-in-cone textures are present in samples 3110R1 and 3110R2 (Figures 2 and 3A). The main mineralogy of sample 3112R1 is HMC, and sample 3112R3 is mainly composed of HMC and aragonite. The latter two samples contain abundant peloids, mollusk fragments, and corrosion seams, apparently reflecting dissolution events (Figure 3E,F and Figure 4F).

4.2. Major and Trace Elements

Major element concentrations of bulk samples and trace element concentrations of carbonate phases are summarized in Tables 2 and 3, respectively. LMC exhibits relatively high Fe (Fe_2O_3: 1.16–3.56 wt %), Mn (MnO: 0.07–0.66 wt %), low Sr (185–512 μg/g), and low to moderate Ba (6–133 μg/g) concentrations. LMC from both sites reveals flat REE patterns with minor middle REE (MREE) enrichment. Sample 3112R1 shows stronger MREE enrichment (Figure 5).

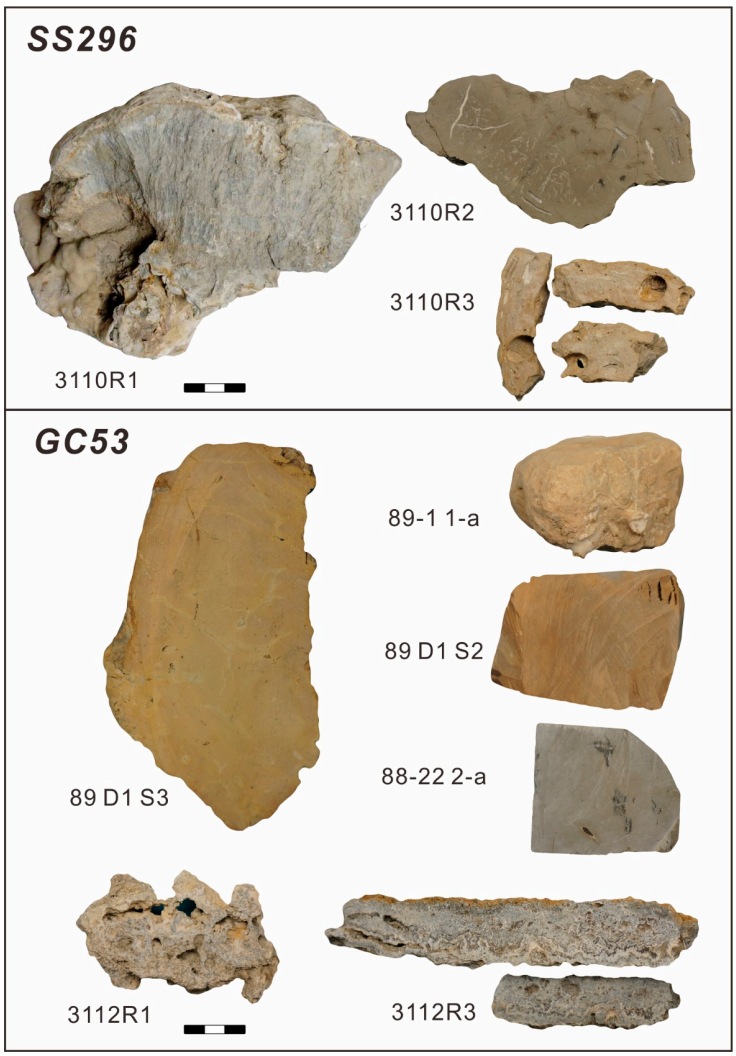

Figure 2. Morphologies of selected carbonate lithologies from sites SS296 and GC53. Carbonates are gray and yellow and exhibit variable morphologies including crusts, slabs, and irregular structures. Presence of cone-in-cone texture in sample 3110R1. Two samples that are composed of high-Mg calcite and aragonite (3112R1, 3112R3) from GC53 are highly porous, while all other samples consist exclusively of low-Mg calcite and exhibit little porosity. Bioclasts are common in the two porous samples but absent in the other samples. The scale bars are 3 cm.

Table 1. Mineral composition of authigenic carbonates from sites SS296 and GC53 of the Gulf of Mexico.

Sample No.	Qtz	LMC	$MgCO_3$ (%)	HMC	$MgCO_3$ (%)	Arag.	Dolo.	Sd
SS296								
3110R1	16	82	4					18
3110R2	12	100	2					
3110R3	14	93	5				7	
GC53								
88–22 2-a	6	89	1					11
89-1 1-a	12	98	1					2
89 D1 S2	5	61	5					39
89 D1 S3	7	100	2					
3112R1				90	10	10		
3112R3	10			45	16	55		

Qtz = quartz; LMC = low-Mg calcite; $MgCO_3$ (%) = mol % $MgCO_3$ in carbonate minerals; HMC = high-Mg calcite; Arag. = aragonite; Dolo. = (proto) dolomite; Sd = siderite.

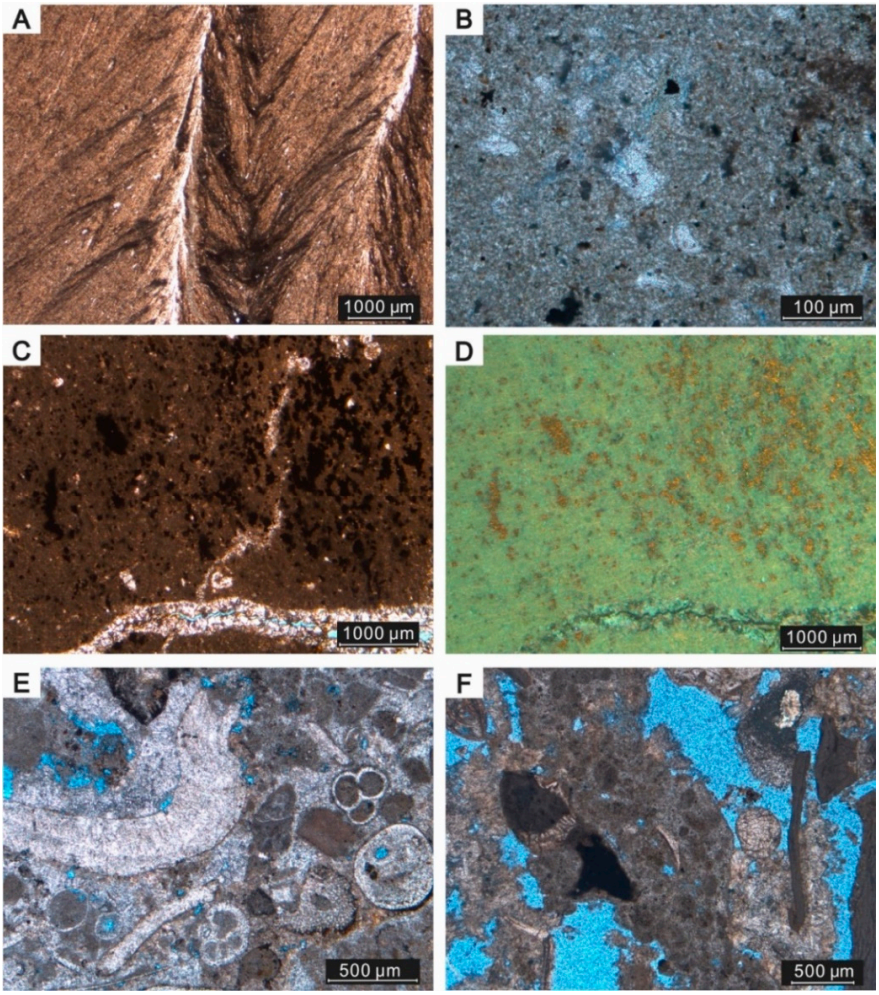

Figure 3. Photomicrographs of typical fabrics of carbonates from sites SS296 (**A**,**B**) and GC53 (**C**–**F**). (**A**) Cone-in-cone calcite (3110R2). (**B**) Microcrystalline low-Mg calcite and organic matter (black; 3110R3). (**C**,**D**) Pyrite (dark) in a micritic, low-Mg calcite matrix; note two generations of veins (light; 89 D1 S3). (**E**,**F**) Peloids, mollusk fragments, and corrosion rims resulting from dissolution are common in the two samples that are composed of aragonite and high-Mg calcite (3112R1, 3112R3). All photographs are plane-polarized light except D, which is a reflected light image.

4.3. Carbonate Carbon and Oxygen Isotopes

$\delta^{13}C$ and $\delta^{18}O$ values of the studied samples are shown in Figure 6 and Table S1. $\delta^{13}C$ values of LMC from site SS296 fall into two groups, ranging from −17.5‰ to −15.1‰ (average: −16.5‰, n = 14) and −10.8‰ to −9.1‰ (average: −10.1‰, n = 8). Similarly, $\delta^{18}O$ values of the LMC from site SS296 can be divided into two groups, ranging from −0.6‰ to 1.7‰ (average: 0.5‰, n = 14) and from 6.3‰ to 7.5‰ (average: 6.9‰, n = 8). Sample 89 D1 S3 from site GC53 yields negative $\delta^{13}C$ values from −14.4‰ to −7.8‰ (average: −11.1‰, n = 6), while other LMC samples from the same site yield higher $\delta^{13}C$ values, ranging from −3.3‰ to 2.6‰ (average: 0.4‰, n = 15). $\delta^{18}O$ values of LMC from site GC53 are negative, ranging from −9.4‰ to −2.5‰ (average: −7.0‰, n = 21). Samples 3112R1 and 3112R3 dominated by HMC and/or aragonite from site GC53 reveal the most negative $\delta^{13}C$ values from −45.3‰ to −15.8‰ (average: −28.6‰, n = 6) and $\delta^{18}O$ values between −1.7‰ and 3.0‰ (average: 1.0‰, n = 6).

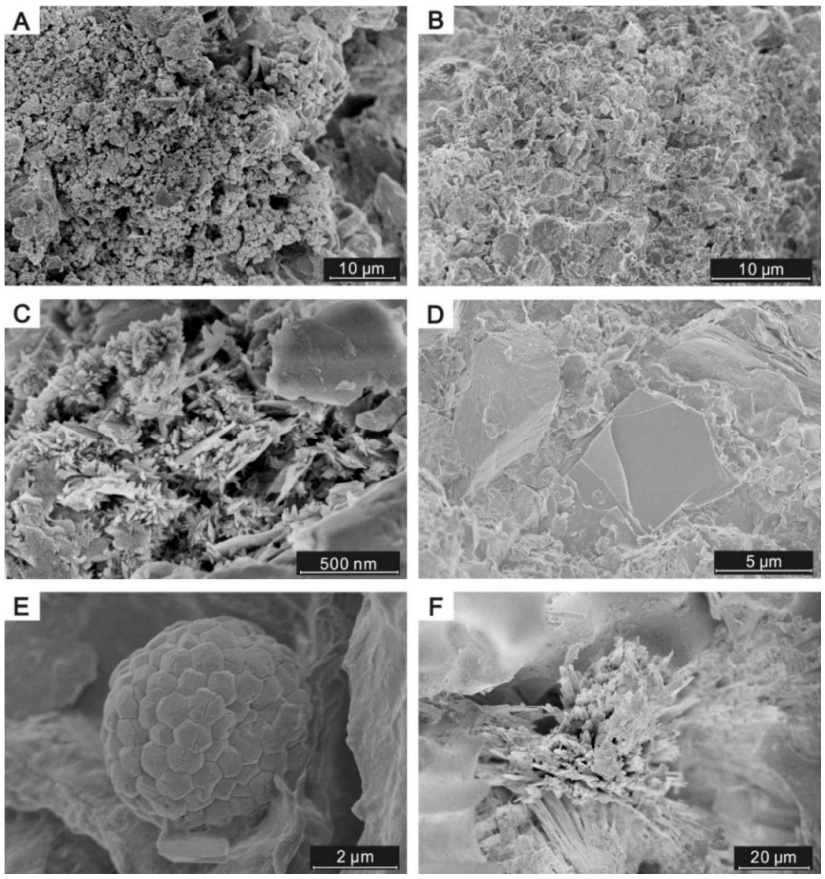

Figure 4. Scanning electron micrographs of representative authigenic carbonates. (**A**,**B**) Microcrystalline subhedral low-Mg calcite (3110R2, 3110R3). (**C**) Rod-shaped aggregates of euhedral low-Mg calcite (89-1 1-a). (**D**) Detrital terrigenous minerals cemented by micritic carbonate (89 D1S2). (**E**) Pyrite framboid enclosed in micritic matrix (3112R1). (**F**) Needle fan aragonite surrounded by bioclasts (3112R3).

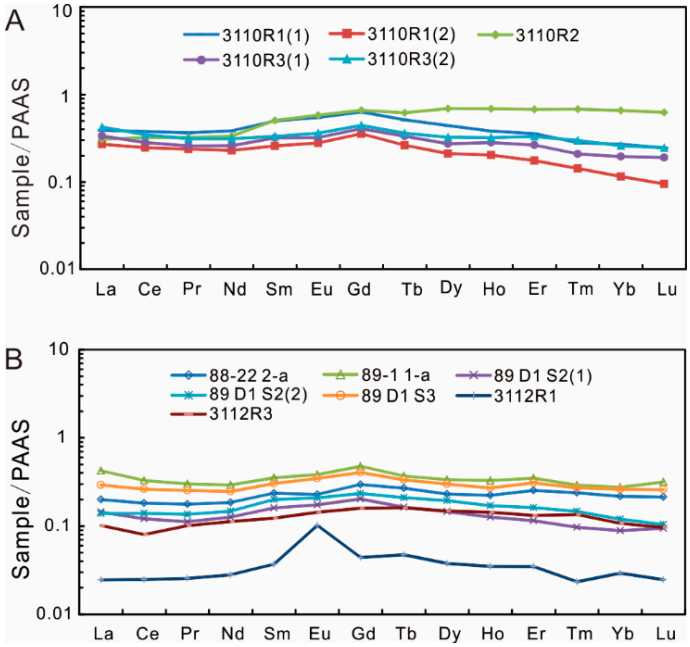

Figure 5. Shale-normalized REE patterns of carbonates from site SS296 (**A**) and site GC53 (**B**).

Table 2. Concentrations of major elements (wt %) in bulk carbonate samples.

Sample	SS296							GC53				
	3110R1(1)	3110R1(2)	3110R2	3110R3(1)	3110R3(2)	88-22 2-a	89-1 1-a	89 D1 S2(1)	89 D1 S2(2)	89 D1 S3	3112R1	3112R3
Na_2O	0.66	0.93	0.65	0.77	0.78	0.63	0.71	0.60	0.69	0.58	0.75	0.77
MgO	2.23	1.87	1.38	1.43	1.56	1.23	1.32	3.90	1.66	1.15	2.59	2.98
Al_2O_3	5.40	4.65	5.01	5.47	4.90	4.39	5.90	3.45	4.78	3.98	0.58	1.71
P_2O_5	0.19	0.37	0.16	0.13	0.12	3.15	0.61	0.62	0.17	0.50	0.16	0.11
K_2O	1.27	1.20	1.14	1.28	1.21	0.97	1.27	0.76	1.04	0.91	0.15	0.39
CaO	26.93	20.81	35.96	32.62	34.86	37.52	32.55	23.39	35.59	38.38	41.53	43.91
TiO_2	0.25	0.23	0.22	0.25	0.22	0.18	0.24	0.17	0.22	0.16	0.03	0.07
MnO	0.34	0.26	0.44	0.34	0.29	0.16	0.13	0.31	0.09	0.41	0.05	0.07
Fe_2O_3	8.87	8.84	1.90	3.90	3.78	5.06	5.15	23.72	5.91	2.71	5.96	1.07

Table 3. Concentrations of rare earth elements (REEs) and trace elements (μg/g) in carbonate phases of the studied carbonates (note that Fe_2O_3 and MnO concentrations are in wt %).

Sample	SS296							GC53				
	3110R1(1)	3110R1(2)	3110R2	3110R3(1)	3110R3(2)	88-22 2-a	89-1 1-a	89 D1 S2(1)	89 D1 S2(2)	89 D1 S3	3112R1	3112R3
La	14.90	10.30	11.80	12.80	16.20	7.66	16.20	5.51	5.31	11.20	0.94	3.88
Ce	30.10	19.70	25.50	22.50	27.60	14.50	26.10	9.62	11.10	20.90	1.98	6.36
Pr	3.22	2.10	2.85	2.28	2.76	1.56	2.66	0.99	1.20	2.24	0.23	0.89
Nd	13.00	7.78	11.30	8.79	10.60	6.28	9.95	4.29	5.00	8.34	0.95	3.82
Sm	2.75	1.43	2.80	1.77	1.84	1.31	1.96	0.89	1.11	1.69	0.21	0.68
Eu	0.59	0.30	0.63	0.35	0.39	0.25	0.41	0.19	0.23	0.38	0.11	0.16
Gd	2.94	1.65	3.08	1.89	2.07	1.38	2.22	0.95	1.10	1.89	0.21	0.75
Tb	0.40	0.20	0.48	0.26	0.28	0.21	0.29	0.13	0.16	0.26	0.04	0.13
Dy	2.07	0.99	3.23	1.28	1.52	1.08	1.57	0.68	0.91	1.40	0.18	0.69
Ho	0.38	0.20	0.68	0.28	0.32	0.22	0.33	0.13	0.17	0.27	0.03	0.14
Er	1.02	0.50	1.93	0.75	0.94	0.72	1.00	0.33	0.46	0.88	0.10	0.38
Tm	0.11	0.06	0.28	0.08	0.12	0.10	0.12	0.04	0.06	0.11	0.01	0.05
Yb	0.76	0.33	1.85	0.55	0.73	0.61	0.78	0.25	0.34	0.74	0.08	0.30
Lu	0.11	0.04	0.27	0.08	0.11	0.09	0.14	0.04	0.05	0.11	0.01	0.04
Y	13.60	7.36	21.10	9.74	12.50	9.11	14.80	5.00	5.43	10.90	1.33	4.85
∑REE	72.35	45.58	66.67	53.66	65.48	35.97	63.71	24.03	27.19	50.41	5.06	18.27
MnO	0.36	0.24	0.66	0.44	0.37	0.20	0.15	0.07	0.07	0.53	0.03	0.05
Fe_2O_3	3.46	2.09	1.16	2.24	2.60	1.61	1.66	3.56	2.95	1.68	0.40	0.41
Sr	288	219	379	252	278	512	350	185	245	373	3300	4010
Ba	133	59	6	8	8	100	53	69	76	22	693	166
Sr/Mn	0.10	0.12	0.07	0.07	0.10	0.33	0.30	0.34	0.45	0.09	12.60	10.31

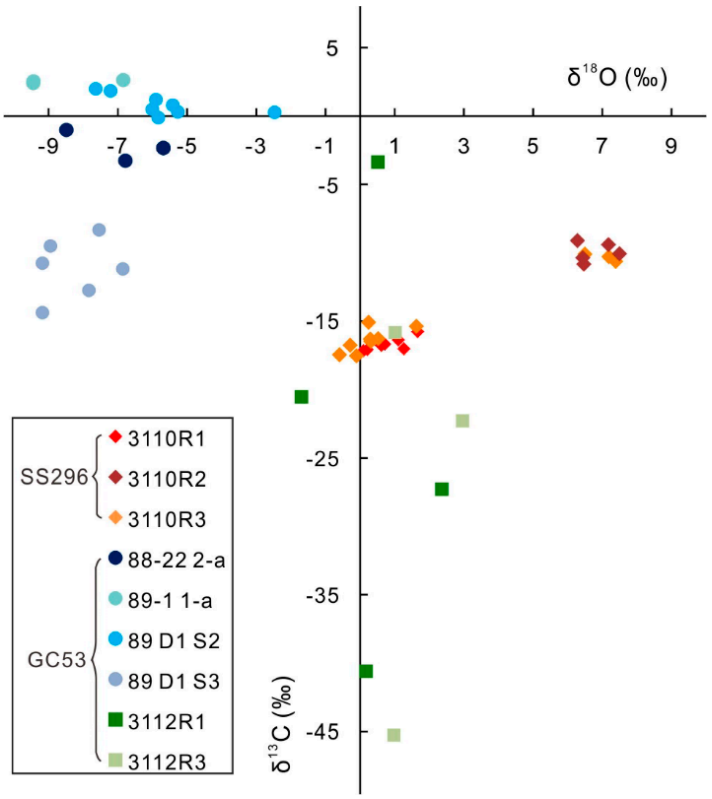

Figure 6. Plot of $\delta^{13}C$ and $\delta^{18}O$ values of carbonates from sites SS296 and GC53 of the Gulf of Mexico.

4.4. Organic Carbon and Nitrogen Concentrations and $\delta^{13}C_{org}$ Values

Average organic carbon concentrations of LMC from sites SS296 and GC53 are 0.25 wt % and 0.21 wt %, respectively (Table S2; Figure 7). These concentrations are slightly lower than the average carbon concentrations of HMC and aragonite samples (0.28 wt %) from site GC53. LMC from both sites has C/N ratios between 6 and 16 with an average of 10.8. C/N ratios of HMC and aragonite samples range from 1 to 7 with an average of approximately 4.4. LMC from both sites yielded similar $\delta^{13}C_{org}$ values, ranging from −26.8‰ to −18.9‰ (average: −24.3‰, n = 33). In contrast, $\delta^{13}C_{org}$ values of samples 3112R1 and 3112R3 are the most negative ones, ranging from −77.2‰ to −53.0‰ (average: −66.7‰, n = 8).

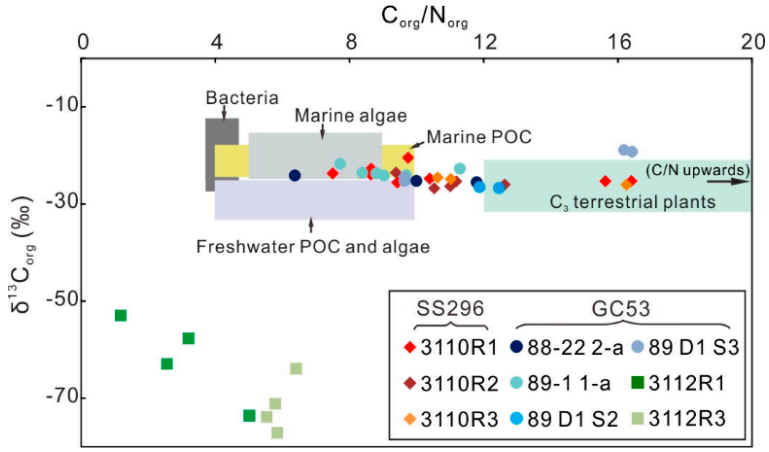

Figure 7. $\delta^{13}C_{org}$ vs. C_{org}/N_{org} of authigenic carbonates. Data fields after Lamb et al. [34]. POC refers to particulate organic carbon.

4.5. Sr Isotopes

$^{87}Sr/^{86}Sr$ ratios of LMC from site SS296 vary between 0.709537 and 0.710537 (Table S1; Figure 8); these ratios are significantly higher than the ratio of modern seawater (0.709175 [35]). LMC from site GC53 exhibits lower $^{87}Sr/^{86}Sr$ ratios ranging from 0.707900 to 0.708498. The $^{87}Sr/^{86}Sr$ ratios of HMC and aragonite from site GC53 vary from 0.708964 to 0.709201, similar to the ratio of modern seawater.

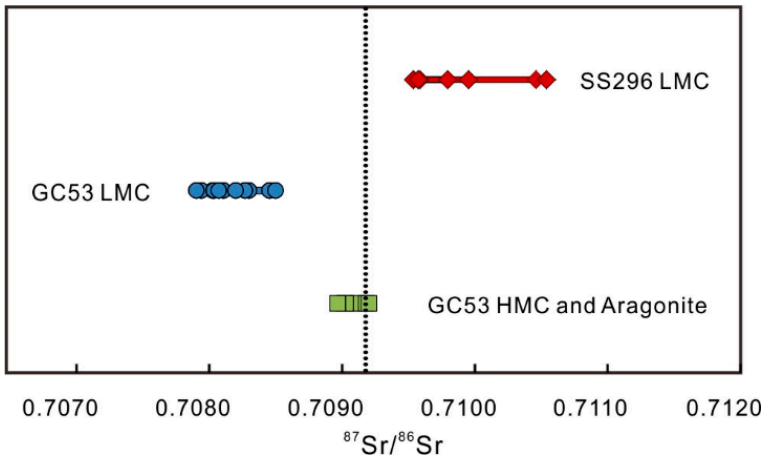

Figure 8. $^{87}Sr/^{86}Sr$ ratios of authigenic carbonates from sites SS296 and GC53. Dashed line corresponds to $^{87}Sr/^{86}Sr$ ratio of modern Gulf of Mexico seawater (0.709175; [35]).

5. Discussion

5.1. Primary Origin of Low-Mg Calcite

Petrographic observations and elemental compositions of the samples from sites SS296 and GC53 reveal that the studied LMC is of primary origin and does not result from recrystallization. It has been shown that petrographic features and geochemical fingerprints (e.g., ghost structures after primary crystals or high Sr concentrations inherited from aragonite precursors) of primary crystals and the transformation process are archived in secondary carbonates [15,16]. Neomorphic carbonate phases resulting from recrystallization usually exhibit different crystal habits such as calcite resulting from pseudomorphic calcitization of aragonite, neomorphic calcite mosaics, and coarse calcite spar [36,37]. The microcrystalline LMC crystals of the studied GoM samples reveal no petrographic evidence for recrystallization (Figures 3A and 4A–D). Additionally, the Sr/Mn ratio tends to decrease upon aragonite transformation to LMC and can consequently be used to recognize the transformation process [38,39]. However, if aragonite converts to calcite under closed system conditions during diagenesis, high Sr or Mg concentrations will be inherited by secondary calcite [6,40]. Accordingly, Buggisch and Krumm [40], Beauchamp and Savard [41], and Peckmann et al. [42] recognized former aragonite through high Sr concentrations in banded and botryoidal calcite cement in ancient hydrocarbon-seep carbonate. The Sr content has also been used to distinguish primary and secondary carbonate phases by Zwicker et al. [6], and a Sr/Mn ratio higher than two has been used to identify samples that are likely to preserve the original Sr isotope composition of ancient seawater in limestones [43]. Upon hypothetical aragonite transformation to calcite, the dense fabric of LMC from both sites would suggest conversion under closed system conditions. In such case, high Sr concentrations would be inherited by secondary LMC. Instead, Sr/Mn ratios of LMC vary from 0.07 to 0.45 and are significantly lower than those of HMC and aragonite (10.31 and 12.60) from site GC53. Its low Sr/Mn ratios (<0.45) and Sr concentrations consequently indicate that LMC from both sites did not result from transformation of aragonite. Therefore, the results suggest that the studied LMC are primary phases and can consequently be used for the reconstruction of fluid sources and formation environments.

5.2. Constraints on the Formation of Low-Mg Calcite

Low Mg/Ca ratios (<2) in fluids are required for the precipitation of LMC [44]. Besides meteoric waters that tend to have low Mg/Ca ratios, marine pore fluids can develop low Mg/Ca ratios by mainly three processes: (1) dissolution of Ca-rich minerals in salt diapirs [22,23,45]; (2) weathering of siliciclastic minerals during shale membrane filtration [23,46]; (3) uptake of Mg and release of Ca during dolomitization [23]. To reveal the fluid sources and formation processes of the studied LMC, we compare the geochemical patterns of LMC from sites SS296 and GC53, which is complemented by a comparison of the LMC phases with HMC and aragonite from site GC53.

5.2.1. Site SS296

Before constraining the conditions of LMC precipitation, isotopic compositions and petrographic characteristics were used to elucidate the environments in which LMC formed. The $\delta^{18}O$ value of authigenic carbonates is a function of the $\delta^{18}O$ value of the fluid, mineralogy, and ambient temperature and has consequently been used to trace fluid sources for carbonate precipitation [11,47–49]. Kim and O'Neil [50] have proposed a formula for calculating the theoretical $\delta^{18}O$ of calcite forming at isotopic equilibrium with ambient fluids:

$$1000 \ln\alpha^{18}O_{\text{calcite-water}} = 18.03 \times 10^3 \, T^{-1} - 32.42 \text{ (“T” is in degree Kelvin).} \quad (1)$$

Equation (1) should be corrected by 0.06‰ per mol % $MgCO_3$ for calcite [51]. In this study, 2.5 mol % $MgCO_3$ in LMC and a $\delta^{18}O$ value of 0.7‰ of bottom seawater (V-SMOW; GC140 [47]) were applied for the calculation of the theoretical $\delta^{18}O$ values of LMC at both study sites. A bottom seawater temperature of 19.9 °C for SS296 (NOAA Open data: cruise: WOD13_US) was inferred, according to bottom water temperatures in adjacent areas. Assuming that LMC from site SS296 formed at the present bottom water temperature, its theoretical $\delta^{18}O$ value is –0.1‰. However, the measured $\delta^{18}O$ values of LMC vary widely and fall into two groups, suggesting that LMC precipitated from fluids of different compositions, at different temperatures, or a combination of both. One group with highly positive $\delta^{18}O$ values suggests precipitation from an ^{18}O-rich fluid. In the inner shelf of the passive continental margin of the GoM, hydrothermal fluids and dissociation of gas hydrate can be excluded as sources of ^{18}O-rich water. As evaporites are widespread in the GoM and hypersaline seawater is enriched in ^{18}O [46] and a salt diapir is present in the buried sediment at site SS296, the formation of LMC with significantly positive $\delta^{18}O$ values is best explained by evaporation-affected seawater trapped in the sedimentary column. Another group with lower $\delta^{18}O$ values is close to the theoretical $\delta^{18}O$ value of LMC at SS296, suggesting the formation in a fluid with a similar composition to modern seawater. However, cone-in-cone textures typify samples 3110R1 and 3110R2, while these samples are among or partly among the samples with lower $\delta^{18}O$ values. A widely accepted explanation for these textures is a formation environment of high hydraulic pressure and increased temperatures during burial [52,53], although a different interpretation of early cementation during shallow burial in marine environments was proposed for these fibrous calcite layers by Greene et al. [54]. Cone-in-cone calcite is commonly believed to form at temperatures between 70 °C and 120 °C and is interpreted to form by (1) force of crystallization or (2) seepage forces induced by fluid overpressure in the subsurface [52,53]. At such high temperatures, the observed relatively high $\delta^{18}O$ values would reflect ^{18}O-enriched fluids. Therefore, we speculated that the two groups of samples from site SS296 defined by different $\delta^{18}O$ values precipitated from a similar pool of pore water but formed at different depths and temperatures.

To test this hypothesis, we calculated the ambient formation temperature of the second group with lower $\delta^{18}O$ values, assuming that the group with higher $\delta^{18}O$ values precipitated at the seafloor. Average $\delta^{18}O$ values of the two groups of sample 3110R2 (0.3‰ and 7.0‰) are substituted in Equation (1), as well as the temperature at the seafloor at site SS296 (19.9 °C). Interestingly, the obtained temperature of 55.9 °C is close to formation temperatures reported for cone-in-cone calcite, agreeing with the interpretation that the two groups of LMC precipitated from pore waters of similar composition.

It has been suggested that diapirism is an important process of material transportation in sediments (e.g., [55]). Therefore, samples 3110R1 and part of 3110R2 with lower $\delta^{18}O$ values were probably brought up from depth with salt diapirism, supported by the presence of a diapir at site SS296.

Based on such interpretation, the question of what process led to low Mg/Ca ratios in pore fluids needs to be addressed. The $^{87}Sr/^{86}Sr$ ratio of pore fluids is affected by the supply and exchange of Sr in sediments, for example by salt dissolution [45] and alteration of silicates [46]. Because the $^{87}Sr/^{86}Sr$ ratio of carbonate archives the ratio of the fluid from which it precipitated [56], it has been used to reconstruct pore fluid composition (e.g., [11,57]). Among others, Peckmann et al. [57] have shown that seep carbonates reveal $^{87}Sr/^{86}Sr$ ratios that are indistinguishable from ambient seawater and concluded that Sr and probably other cations typically derive from a shallow source at marine seeps. In accord with less radiogenic Sr compositions of marine bottom water in the geologic past, Tong et al. [12] and Naehr et al. [7] suggested that lower $^{87}Sr/^{86}Sr$ ratios in seep carbonates derive from older pore fluids from greater depth. Compared to modern seawater, buried evaporated seawater should have originally exhibited lower $^{87}Sr/^{86}Sr$ ratios due to the lower $^{87}Sr/^{86}Sr$ ratio of ancient seawater since the Ordovician [37]. However, LMC from site SS296 reveals a radiogenic Sr isotope composition. Such radiogenic Sr is possibly ascribed to the supply of Sr from weathering of siliciclastic sediments, which would release Ba, Ca, and radiogenic Sr to the fluid (e.g., [58–60]). Louann salt, as well as the associated calcite and anhydrite, reveal a wide range of $^{87}Sr/^{86}Sr$ ratios due to the mixture of original unradiogenic Sr from Jurassic seawater and radiogenic Sr from siliciclastics [19,61,62]. Radiogenic Sr is released during alteration of silicate minerals within deeply buried sediments [62], and such Sr was apparently taken up by the Louann salt and associated secondary calcite and anhydrite. Based on the Rb/Sr analyses of salt, anhydrite, and fluid inclusions, as well as Sr isotope composition ($^{87}Sr/^{86}Sr > 0.71000$) analyses, Land et al. [19] suggested that diagenesis has been an ongoing process in the bittern zone, involving formation waters (evaporated seawater or coeval fluid) that have experienced considerable water–rock interaction with silicate minerals. Therefore, the high $^{87}Sr/^{86}Sr$ ratio of SS296 LMC could also reflect radiogenic Sr derived from the Louann salt.

Trace elements in carbonate minerals have been used to recronstruct formation environments and fluid sources. Compared to HMC and aragonite from site GC53 in this study and HMC (Mean: Mn: 0.07 wt %; Sr: 1103 μg/g; Ba: 23.03 μg/g) from the South China Sea [63], LMC from site SS296 is depleted in Sr and enriched in Fe and Mn, as well as typified by low to moderate Ba conents (Table 3; Figure 9). Low strontium concentrations in carbonate phases with radiogenic $^{87}Sr/^{86}Sr$ ratios are more likely ascribed to exchange of Sr rather than Sr supply from the weathering of surrounding siliciclastic sediments. The interpretation is also supported by low to moderate Ba concentrations in LMC. We suggest that Fe and Mn enrichment in SS296 LMC resulted from high Fe and Mn concentrations of the pore fluids from which LMC prepipitated. The flat REE pattern of LMC (Figure 5) suggests that Fe enrichment in pore fluid does not result from Fe reduction, which would increase Fe^{2+} concentration coupled with an enrichment of middle REEs in pore fluids [64]. Iron and Mn enrichment of LMC are consistent with the high Fe and Mn concentrations in saline fluids reported by Fu and Aharon [45] and Aharon et al. [22], which was ascribed to Fe and Mn contained in underlying evaporites [22]. Additionally, Prikryl et al. [65] reported similar Fe and Mn enrichment in salt dome calcite, although Fe enrichment is due to the abundance of pyrite in micrite in this case. Taken together, these observations indicate that radiogenic Sr most likely resulted from element exchange with the local salt structure through salt dissolution coupled with elemental redistribution between anhydrite and gypsum and the surrounding strata. The low Mg/Ca ratio required for LMC precipitation consequently resulted from the partial dissolution of the salt diapir that later on played a critical role in transporting the LMC-containing lithologies to the seafloor.

The analysis of carbon sources helps to better understand the formation process of LMC. The carbon in authigenic carbonates could derive from seawater ($\delta^{13}C = 0 \pm 3‰$; [66]), the oxidation of organic matter ($\delta^{13}C$ approximately −25‰ [67]), methane (microbial methane: $\delta^{13}C$: −110‰ to −50‰; thermogenic methane: $\delta^{13}C$: −50‰ to −20‰), and crude oil ($\delta^{13}C$: −35‰ to −25‰) [30]. The ambient

carbon pools are also utilized by different microbial and macro-organisms (e.g., [68,69]). Thus, $\delta^{13}C$ and $\delta^{13}C_{org}$ values of carbonates were applied to reconstruct carbon sources and biogeochemical cycling of carbon (cf. [11,34,48,70]). The $\delta^{13}C_{org}$ values of LMC are similar to those of marine sediments, reflecting a mixture of terrigenous and marine organic matter [34], and revealing no evidence of a ^{13}C-depleted carbon source like at hydrocarbon seeps [70]. Moreover, its only moderately negative $\delta^{13}C$ values indicate that LMC mostly contains carbon derived from organoclastic sulfate reduction (OSR) with marine organic matter as electron donor rather than carbon derived from methane oxidation. The lack of evidence for pore waters with seawater-like $\delta^{13}C$ signature suggests that the LMC formed at greater depth in sediments without seawater ingress. Therefore, the formation temperatures of LMC with significantly positive $\delta^{18}O$ could be higher than the temperature at the seafloor, suggesting a higher formation temperature of LMC with lower $\delta^{18}O$ values than the calculated temperature of 55.9 °C. Because salt diapirs contain anhydrite and gypsum, partial dissolution of the diapir could have been an additional source of sulfate for OSR driving LMC formation at depth [61,62,71].

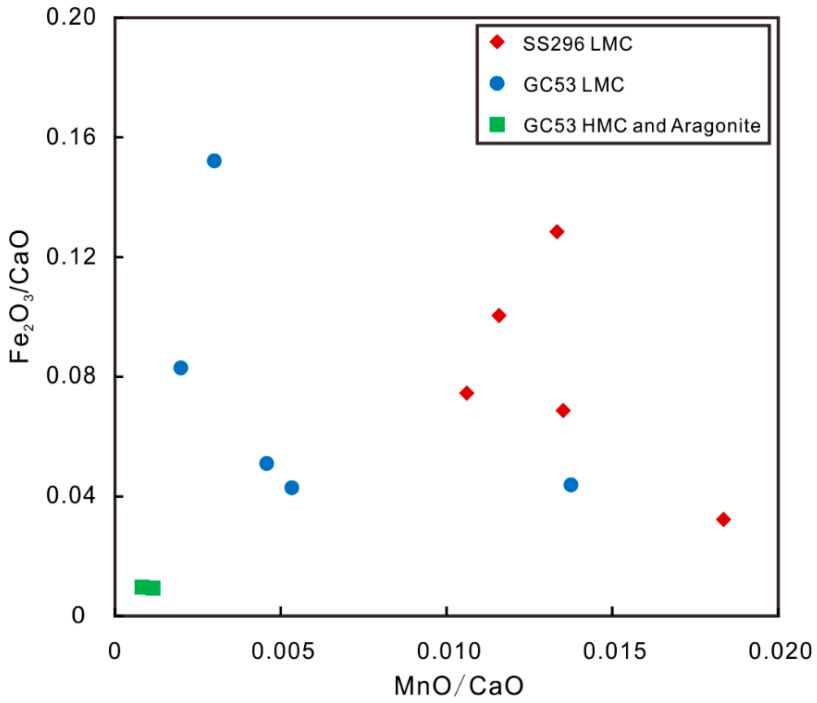

Figure 9. Fe_2O_3/CaO and MnO/CaO ratios of authigenic carbonates from sites SS296 and GC53. Concentrations are in wt % for Fe_2O_3, MnO, and CaO.

5.2.2. Site GC53

LMC recovered at site GC53 reveals significantly negative $\delta^{18}O$ values, compared to the higher $\delta^{18}O$ values of HMC and aragonite from the same site. The calculated equilibrium $\delta^{18}O$ value is 1.1‰ for LMC using a local bottom water temperature of 14.5 °C [72]. At the present bottom water temperature, the $\delta^{18}O$ value of a fluid required for LMC formation can be as low as −9.9‰ (V-SMOW). Continental groundwater entrenched in offshore sediments can provide ^{18}O-depleted fluid, but the $\delta^{18}O$ value of present groundwater in Louisiana is only as low as −6.0‰ (V-SMOW; [73]). Therefore, the fluid from which LMC precipitated could have had a more negative $\delta^{18}O$ value than the present groundwater. A possible candidate is ancient entrenched groundwater, which can reveal more negative $\delta^{18}O$ values during periods of lower sea level [24,74]. Joye et al. [10] reported hot (>40 °C) seep brine in a mud volcano from site GB425, implying that the seep fluid at site GC53 might be relatively hot. Such elevated temperature could explain the $\delta^{18}O$ offset between the theoretic fluid and present groundwater. Hence, the fluid from which LMC precipitated could have been ancient groundwater or present, hot groundwater.

Meteoric water along the Gulf Coast usually exhibits radiogenic Sr isotope composition due to alteration of siliciclastic minerals, deriving from the weathering of continental rocks with a radiogenic Sr composition [75,76]. However, $^{87}Sr/^{86}Sr$ ratios of GC53 LMC are significantly lower than those of modern seawater, suggesting that Sr isotope compositions of meteoric water have been modified by pore fluid–sediment interactions. Similar to LMC at site SS296 influenced by salt dissolusion, LMC at site GC53 reveals flat REE patterns, Fe and Mn enrichment, and Sr depletion, as well as low to moderate Ba concentrations, very different from sample 3112R1 dominated by HMC and sample 3112R3 dominated by HMC and aragonite. Although Mn concentrations in some samples of LMC from GC53 are slightly enriched, Mn concentrations are still consistent with $\delta^{13}C$ values close to that of marine dissolved inorganic carbon (DIC), suggesting an influence of seawater. The altered $^{87}Sr/^{86}Sr$ ratios of LMC are ascribed to salt dissolution, which can produce a wide range of $^{87}Sr/^{86}Sr$ ratios [19,61,62]. Therefore, the unradiogenic Sr in LMC from site GC53 is most likely ascribed to a salt diapir that contains more original Sr from the Jurassic salt, a pattern that is common in salt structures and salt-derived fluids in the GoM [45,77]. Accordingly, salt dissolution coupled to element redistribution among anhydrite and gypsum and the surrounding sediments is the most likely process that resulted in a low Mg/Ca ratios of pore fluids that favored the precipition of LMC.

HMC and aragonite from site GC53 reveal significantly negative $\delta^{13}C$ values typical of seep carbonates, which results from the incorporation of ^{13}C-depleted carbon deriving from oil or methane [11,57]. Such an interpretation is confirmed by the $\delta^{13}C_{org}$ values as low as −77.2‰ of HMC and aragonite. Additionally, the abundant bioskeletal components and microfabrics of these two samples are similar to other seep carbonates (Figure 3E,F and Figure 4F) [47]. In sharp contrast, LMC from site GC53 yields $\delta^{13}C_{org}$ values similar to that of LMC from site SS296 (Figure 7) and higher $\delta^{13}C$ values, indicating mixed carbon sources of seawater DIC and organic matter. Among LMC lithologies from site GC53, sample 89 D1 S3 reveals the most negative $\delta^{13}C$ values and contains abundant pyrite, indicating marine DIC and carbon species derived from OSR as main carbon sources. Other LMC from site GC53 reveals $\delta^{13}C$ values similar to that of DIC of modern seawater, indicating that seawater DIC is the main carbon source, which is consistent with the low Mn content of LMC (Table 3; Figure 9). Because fluids tend to be Ca^{2+}-enriched after interaction with salt diapirs [5,10,22,45], LMC apparently precipitated from seawater DIC but only after the interaction of pore fluids with the Louann salt.

Overall, LMC from sites SS296 and GC53 reveals contrasting geochemical signatures. However, at both sites, LMC precipitated from fluids inheriting low Mg/Ca ratios through salt dissolution. LMC from site SS296 precipitated from a fluid affected by salt dissolution, after the alkalinity of the fluid was increased by OSR. LMC from GC53 possibly precipitated from ancient groundwater in the subsurface near to the seafloor with marine DIC as a main carbon source, and in the case of one sample (89 D1 S3) with a contribution of carbonate species derived from OSR.

5.3. Implications of the Occurrence of Low-Mg Calcite in Marine Settings

Different formation mechanisms of LMC in marine sediments during times of an aragonite sea have been recognized. LMC from Monterey Bay most likely formed under the local influence of meteoric water [7]. While LMC at sites SS296 and GC53 apparently precipitated due to low Mg/Ca ratios in fluids resulting from salt dissolution, in some instances the presence of meteoric water may have contributed to LMC formation. Similarly, the precipitation of LMC at a water depth of 2330 m at site AC601 in the GoM has been ascribed to a low Mg/Ca ratio in the local brine pool [5] that is typically related to salt diapirism in the subsurface [78]. However, the carbon sources of LMC from site AC601 are mostly hydrocarbons contained in seep fluids rather than sedimentary organic matter or seawater DIC, which are the main carbon sources of the LMC samples studied herein. Similar seafloor occurrences of LMC have been found at more than 10 other hydrocarbon seeps [5,8,9]. The presence of sulfate-driven anaerobic oxidation of hydrocarbons alters pore fluid composition but tends to cause higher Mg/Ca ratios in pore waters due to the precipitation of aragonite and HMC [6,64]—a trend that

does not favor LMC formation but does rather favor dolomite formation [79]. We put forward the hypothesis that the interaction of pore fluids with salt deposits is the main mechanism that causes precipitation of LMC in marine sediments, whereas precipitation under the influence of meteoric waters seems to be a subordinate factor, at least in the GoM. Clearly more work is needed to understand the factors governing LMC formation, and both seep and non-seep environments of the GoM should be studied in the future. Due to the widespread occurrence of salt structures in marginal seas around the world, the formation of LMC may be more common in marine sediments than previosuly recognized even during the current aragonite sea mode of the ocean. Our results may provide the means to distinguish different types of LMC in the geologic record as well as the basis for a better understanding of the information archived in primary LMC.

6. Conclusions

Through petrographic and trace element analyses, we demonstrate that low-magnesium calcite (LMC) from sites SS296 and GC53 of the Gulf of Mexico is of primary origin. At both sites, the low Mg/Ca ratios of pore fluids required for LMC precipitation most likely originated from salt dissolution, as indicated by the high Fe and Mn as well as low Sr concentrations of LMC and its widely varying $^{87}Sr/^{86}Sr$ ratios. It is suggested that salt dissolution came along with the migration of hypersaline pore waters (site SS296) and entrenched groundwater (site GC53), favoring LMC formation. The high carbonate alkalinity required for LMC precipitation was generated from a combination of dissolved inorganic carbon (DIC) from seawater and organoclastic sulfate reduction (OSR) as indicated by moderately negative $\delta^{13}C$ values, and $\delta^{13}C_{org}$ values that are similar to those of sedimentary organic matter. We hypothesize that primary LMC related to the partial dissolution of subsurface salt deposits is possibly more common than previously recognized, given the common occurrence of salt diapirs along continental margins. This study may consequently provide the means to interpret some occurrences of LMC in the geologic record, setting the stage for the application of this stable geological archive in paleoenvironment reconstruction.

Supplementary Materials: The following files are available online at http://www.mdpi.com/2075-163X/9/4/251/s1. Figure S1: XRD patterns of selected carbonates from the Gulf of Mexico analyzed in this study. Table S1: Carbon, oxygen, and strontium isotopic compositions of authigenic carbonates from sites SS296 and GC53. Table S2: Carbon isotopic compositions of organic matter, C and N concentrations, and C/N ratios of the authigenic carbonates from sites SS296 and GC53.

Author Contributions: Conceptualization: D.F. and H.H; methodology: H.H.; formal analysis: H.H., S.G., N.L., and M.C.; investigation: H.H.; resources: H.H.; data curation: H.H.; writing—original draft preparation: H.H., S.G., N.L., D.B., J.P., H.H.R., D.C., and D.F.; writing—review and editing: H.H., S.G., N.L., M.J., D.B., J.P., and D.F.; visualization: H.H.; supervision: D.F.; project administration: D.F.; funding acquisition: D.F.

Funding: This research was partially supported by the National Key R&D Program of China (2018YFC0310004), the National Program on Global Change and Air-Sea Interaction (Grant no: GASI-GEOGE-05-04), the NSF of China (Grants: 41761134084 and 41730528), and the Deutsche Forschungsgemeinschaft (PE 847/7-1).

Acknowledgments: Samples were collected during projects funded by the U.S. Bureau of Ocean Energy Management and the National Oceanic and Atmospheric Administration's National Undersea Research Program. We are grateful to Y.B. Peng (LSU) for stable isotope measurements. Insightful comments by three anonymous reviewers helped improve the manuscript.

Conflicts of Interest: The authors declare that they have no conflicts of interest regarding the publication of this paper.

References

1. Hardie, L.A. Secular variation in seawater chemistry: An explanation for the coupled secular variation in the mineralogies of marine limestones and potash evaporites over the past 600 m.y. *Geology* **1996**, *24*, 279–283. [CrossRef]
2. Lowenstein, T.K.; Timofeeff, M.N.; Brennan, S.T.; Hardie, L.A.; Demicco, R.V. Oscillations in Phanerozoic seawater chemistry: Evidence from fluid Inclusions. *Science* **2001**, *294*, 1086–1088. [CrossRef] [PubMed]

3. Stanley, S.M.; Ries, J.B.; Hardie, L.A. Low-magnesium calcite produced by coralline algae in seawater of Late Cretaceous composition. *Proc. Natl. Acad. Sci. USA* **2002**, *99*, 15323–15326. [CrossRef] [PubMed]
4. Burton, E.A.; Walter, L.M. The effects of pCO_2 and temperature on magnesium incorporation in calcite in seawater and $MgCl_2$-$CaCl_2$ solutions. *Geochim. Cosmochim. Acta* **1991**, *55*, 777–785. [CrossRef]
5. Feng, D.; Roberts, H.H.; Joye, S.B.; Heydari, E. Formation of low-magnesium calcite at cold seeps in an aragonite sea. *Terra Nova* **2014**, *26*, 150–156. [CrossRef]
6. Zwicker, J.; Smrzka, D.; Himmler, T.; Monien, P.; Gier, S.; Goedert, J.L.; Peckmann, J. Rare earth elements as tracers for microbial activity and early diagenesis: A new perspective from carbonate cements of ancient methane-seep deposits. *Chem. Geol.* **2018**, *501*, 77–85. [CrossRef]
7. Naehr, T.H.; Eichhubl, P.; Orphan, V.J.; Hovland, M.; Paull, C.K.; Ussler, W.; Lorenson, T.D.; Greene, H.G. Authigenic carbonate formation at hydrocarbon seeps in continental margin sediments: A comparative study. *Deep Sea Res. Part II* **2007**, *54*, 1268–1291. [CrossRef]
8. Hu, Y.; Feng, D.; Peckmann, J.; Roberts, H.H.; Chen, D. New insights into cerium anomalies and mechanisms of trace metal enrichment in authigenic carbonate from hydrocarbon seeps. *Chem. Geol.* **2014**, *381*, 55–66. [CrossRef]
9. Feng, D.; Peng, Y.; Bao, H.; Peckmann, J.; Roberts, H.H.; Chen, D. A carbonate-based proxy for sulfate-driven anaerobic oxidation of methane. *Geology* **2016**, *44*, 999–1002. [CrossRef]
10. Joye, S.B.; MacDonald, I.R.; Montoya, J.P.; Peccini, M. Geophysical and geochemical signatures of Gulf of Mexico seafloor brines. *Biogeosciences* **2005**, *2*, 295–309. [CrossRef]
11. Greinert, J.; Bohrmann, G.; Suess, E. Gas hydrate-associated carbonates and methane-venting at Hydrate Ridge: Classification, distribution, and origin of authigenic lithologies. *Nat. Gas Hydrates Occur. Distrib. Detect.* **2001**, *124*, 99–113. [CrossRef]
12. Tong, H.; Feng, D.; Cheng, H.; Yang, S.; Wang, H.; Min, A.G.; Edwards, R.L.; Chen, Z.; Chen, D. Authigenic carbonates from seeps on the northern continental slope of the South China Sea: New insights into fluid sources and geochronology. *Mar. Pet. Geol.* **2013**, *43*, 260–271. [CrossRef]
13. Gomberg, D.N.; Bonatti, E. High-magnesian calcite: Leaching of magnesium in the deep sea. *Science* **1970**, *168*, 1451–1453. [CrossRef] [PubMed]
14. Johnson, W.J.; Goldstein, R.H. Cambrian sea water preserved as inclusions in marine low-magnesium calcite cement. *Nature* **1993**, *362*, 335–337. [CrossRef]
15. Budd, D.A. Petrographic products of freshwater diagenesis in Holocene ooid sands, Schooner Cays, Bahamas. *Carbonates Evaporites* **1988**, *3*, 143–163. [CrossRef]
16. Frank, T.D.; Lohmann, K.C. Diagenesis of fibrous magnesian calcite marine cement: Implications for the interpretation of $\delta^{18}O$ and $\delta^{13}C$ values of ancient equivalents. *Geochim. Cosmochim. Acta* **1996**, *60*, 2427–2436. [CrossRef]
17. Salvador, A. Late Triassic- Jurassic paleogeography and origin of Gulf of Mexico basin. *AAPG Bull.* **1987**, *71*, 419–451. [CrossRef]
18. Woodbury, H.O.; Murry, I.B.; Pickford, P.J. Pliocene and Pleistocene depocenters, outer continental shelf, Louisiana and Texas. *AAPG Bull.* **1973**, *57*, 2428–2439.
19. Land, L.S.; Eustice, R.A.; Mack, L.E.; Horita, J. Reactivity of evaporites during burial: An example from the Jurassic of Alabama. *Geochim. Cosmochim. Acta* **1995**, *59*, 3765–3778. [CrossRef]
20. Sassen, R.; Cole, G.A.; Drozd, R.; Roberts, H.H. Oligocene to Holocene hydrocarbon migration and salt-dome carbonates, northern Gulf of Mexico. *Mar. Pet. Geol.* **1994**, *11*, 55–65. [CrossRef]
21. Stueber, A.M.; Walter, L.M. Origin and chemical evolution of formation waters from Silurian-Devonian strata in the Illinois basin, USA. *Geochim. Cosmochim. Acta* **1991**, *55*, 309–325. [CrossRef]
22. Aharon, P.; Roberts, H.H.; Snelling, R. Submarine venting of brines in the deep Gulf of Mexico: observations and geochemistry. *Geology* **1992**, *20*, 483–486. [CrossRef]
23. Land, L.S. NaCaCl saline formation waters, Frio Formation (Oligocene), south Texas, USA: Products of diagenesis. *Geochim. Cosmochim. Acta* **1995**, *59*, 2163–2174. [CrossRef]
24. Cohen, D.; Person, M.; Wang, P.; Gable, C.W.; Hutchinson, D.; Marksamer, A.; Dugan, B.; Kooi, H.; Groen, K.; Lizarralde, D.; et al. Origin and extent of fresh paleowaters on the Atlantic continental shelf, USA. *Ground Water* **2010**, *48*, 143–158. [CrossRef]
25. Posey, H.H.; Kyle, J.R. Fluid-rock interactions in the salt dome environment: An introduction and review. *Chem. Geol.* **1988**, *74*, 1–24. [CrossRef]

26. Beckman, J.D.; Williamson, A.K. *Salt-dome Locations in the Gulf Coastal Plain, South-Central United States*; Center for Integrated Data Analytics Wisconsin Science Center: Austin, TX, USA, 1990.
27. Roberts, H.H.; Sassen, R.; Carney, R.; Aharon, P. Carbonate buildups on the continental slope off central Louisiana. *Offshore Technol. Conf.* **1989**, *5953*, 655–662.
28. Christopher, K.S.; Joel, W.S. Geometry and development of the salt withdrawal basin in Ship Shoal Block 318 and vicinity. *Gulf Coast Assoc. Geol. Soc. Trans.* **1998**, *48*, 173–180.
29. Cook, D.; D'Onfro, P. Jolliet field thrust fault structure and stratigraphy Green Canyon Block 184, Offshore Louisiana. *Gulf Coast Assoc. Geol. Soc. Trans.* **1991**, *41*, 100–121.
30. Roberts, H.H.; Aharon, P. Hydrocarbon-derived carbonate buildups of the northern Gulf-of-Mexico continental-slope—A review of submersible investigations. *Geo-Mar. Lett.* **1994**, *14*, 135–148. [CrossRef]
31. Sassen, R.; Roberts, H.H.; Aharon, P.; Larkin, J.; Chinn, E.W.; Carney, R. Chemosynthetic bacterial mats at cold hydrocarbon seeps, Gulf of Mexico continental slope. *Org. Geochem.* **1993**, *20*, 77–89. [CrossRef]
32. Goldsmith, J.R.; Graf, D.L.; Heard, H.L. Lattice constants of the calcium-magnesium carbonates. *Am. Mineral.* **1961**, *46*, 453–457.
33. McLennan, S.M. Rare earth elements in sedimentary rocks: Influence of provenance and sedimentary processes. *Rev. Mineral.* **1989**, *21*, 169–200.
34. Lamb, A.L.; Wilson, G.P.; Leng, M.J. A review of coastal palaeoclimate and relative sea-level reconstructions using $\delta^{13}C$ and C/N ratios in organic material. *Earth Sci. Rev.* **2006**, *75*, 29–57. [CrossRef]
35. Paytan, A.; Kastner, M.; Martin, E.E.; Macdougall, J.D.; Herbert, T. Marine barite as a monitor of seawater strontium isotope composition. *Nature* **1993**, *366*, 445–449. [CrossRef]
36. Sandberg, P.A. An oscillating trend in Phanerozoic non-skeletal carbonate mineralogy. *Nature* **1983**, *305*, 19–22. [CrossRef]
37. Denison, R.E.; Koepnick, R.B.; Burke, W.H.; Hetherington, E.A. Construction of the Cambrian and Ordovician seawater $^{87}Sr/^{86}Sr$ curve. *Chem. Geol.* **1998**, *152*, 325–340. [CrossRef]
38. Brand, U. Carbon, oxygen and strontium isotopes in Paleozoic carbonate components: An evaluation of original seawater-chemistry proxies. *Chem. Geol.* **2004**, *204*, 23–44. [CrossRef]
39. Savard, M.M.; Beauchamp, B.; Veizer, J. Significance of aragonite cements around Cretaceous marine methane seeps. *J. Sediment. Res.* **1996**, *66*, 430–438. [CrossRef]
40. Buggisch, W.; Krumm, S. Palaeozoic cold seep carbonates from Europe and North Africa—An integrated isotopic and geochemical approach. *Facies* **2005**, *51*, 566–583. [CrossRef]
41. Beauchamp, B.; Savard, M. Cretaceous chemosynthetic carbonate mounds in the Canadian Arctic. *Palaios* **1992**, *7*, 434–450. [CrossRef]
42. Peckmann, J.; Campbell, K.A.; Walliser, O.H.; Reitner, J. A Late Devonian hydrocarbon-seep deposit dominated by dimerelloid brachiopods, Morocco. *Palaios* **2007**, *22*, 114–122. [CrossRef]
43. Denison, R.E.; Koepnick, R.B.; Fletcher, A.; Howell, M.W.; Callaway, W.S. Criteria for the retention of original seawater $^{87}Sr/^{86}Sr$ in ancient shelf limestones. *Chem. Geol.* **1994**, *112*, 131–143. [CrossRef]
44. Morse, J.W.; Wang, Q.; Tsio, M.Y. Influences of temperature and Mg:Ca ratio on $CaCO_3$ precipitates from seawater. *Geology* **1997**, *25*, 85–87. [CrossRef]
45. Fu, B.; Aharon, P. Sources of hydrocarbon-rich fluids advecting on the seafloor in the northern Gulf of Mexico. *Gulf Coast Assoc. Geol. Soc. Trans.* **1998**, *48*, 73–82.
46. Kharaka, Y.K.; Hanor, J.S. Deep fluids in sedimentary basins. In *Treatise on Geochemistry*, 2nd ed.; Elsevier: Amsterdam, The Netherlands, 2014; pp. 471–515. [CrossRef]
47. Bian, Y.; Feng, D.; Roberts, H.H.; Chen, D. Tracing the evolution of seep fluids from authigenic carbonates: Green Canyon, northern Gulf of Mexico. *Mar. Pet. Geol.* **2013**, *44*, 71–81. [CrossRef]
48. Himmler, T.; Birgel, D.; Bayon, G.; Pape, T.; Ge, L.; Bohrmann, G.; Peckmann, J. Formation of seep carbonates along the Makran convergent margin, northern Arabian Sea and a molecular and isotopic approach to constrain the carbon isotopic composition of parent methane. *Chem. Geol.* **2015**, *415*, 102–117. [CrossRef]
49. Birgel, D.; Feng, D.; Roberts, H.H.; Peckmann, J. Changing redox conditions at cold seeps as revealed by authigenic carbonates from Alaminos Canyon, northern Gulf of Mexico. *Chem. Geol.* **2011**, *285*, 82–96. [CrossRef]
50. Kim, S.T.; O'Neil, J.R. Equilibrium and nonequilibrium oxygen isotope effects in synthetic carbonates. *Geochim. Cosmochim. Acta* **1997**, *61*, 3461–3475. [CrossRef]

51. Tarutani, T.; Clayton, R.N.; Mayeda, T.K. The effect of polymorphism and magnesium substitution on oxygen isotope fractionation between calcium carbonate and water. *Geochim. Cosmochim. Acta* **1969**, *33*, 987–996. [CrossRef]
52. Cobbold, P.R.; Zanella, A.; Rodrigues, N.; Løseth, H. Bedding-parallel fibrous veins (beef and cone-in-cone): Worldwide occurrence and possible significance in terms of fluid overpressure, hydrocarbon generation and mineralization. *Mar. Pet. Geol.* **2013**, *43*, 1–20. [CrossRef]
53. Kershaw, S.; Guo, L. Beef and cone-in-cone calcite fibrous cements associated with the end-Permian and end-Triassic mass extinctions: Reassessment of processes of formation. *J. Palaeogeogr.* **2016**, *5*, 28–42. [CrossRef]
54. Greene, S.E.; Bottjer, D.J.; Corsetti, F.A.; Berelson, W.M.; Zonneveld, J.P. A subseafloor carbonate factory across the Triassic-Jurassic transition. *Geology* **2012**, *40*, 1043–1046. [CrossRef]
55. Omosanya, K.O.; Alves, T.M. Ramps and flats of mass-transport deposits (MTDs) as markers of seafloor strain on the flanks of rising diapirs (Espírito Santo Basin, SE Brazil). *Mar. Geol.* **2013**, *340*, 82–97. [CrossRef]
56. Faure, G. *Principles of Isotope Geology*, 2nd ed.; Smith and Wyllie Intermediate Geology Series; Wiley: New York, NY, USA, 1986.
57. Peckmann, J.; Reimer, A.; Luth, U.; Luth, C.; Hansen, B.T.; Heinicke, C.; Hoefs, J.; Reitner, J. Methane-derived carbonates and authigenic pyrite from the northwestern Black Sea. *Mar. Geol.* **2001**, *177*, 129–150. [CrossRef]
58. Osborn, S.G.; McIntosh, J.C.; Hanor, J.S.; Biddulph, D. Iodine-129, $^{87}Sr/^{86}Sr$, and trace elemental geochemistry of northern Appalachian Basin brines: Evidence for basinal-scale fluid migration and clay mineral diagenesis. *Am. J. Sci.* **2012**, *312*, 263–287. [CrossRef]
59. Kim, J.H.; Torres, M.E.; Haley, B.A.; Ryu, J.S.; Park, M.H.; Hong, W.L.; Choi, J. Marine silicate weathering in the anoxic sediment of the Ulleung Basin: Evidence and consequences. *Geochem. Geophy. Geosy.* **2016**, *17*, 3437–3453. [CrossRef]
60. Li, Y.P.; Jiang, S.Y. Sr isotopic compositions of the interstitial water and carbonate from two basins in the Gulf of Mexico: Implications for fluid flow and origin. *Chem. Geol.* **2016**, *439*, 43–51. [CrossRef]
61. Posey, H.H.; Richard Kyle, J.; Jackson, T.J.; Hurst, S.D.; Price, P.E. Multiple fluid components of salt diapirs and salt dome cap rocks, Gulf Coast, U.S.A. *Appl. Geochem.* **1987**, *2*, 523–534. [CrossRef]
62. Land, L.S.; Kupecz, J.A.; Mack, L.E. Louann salt geochemistry (Gulf of Mexico sedimentary basin, U.S.A.): A preliminary synthesis. *Chem. Geol.* **1988**, *74*, 25–35. [CrossRef]
63. Ge, L.; Jiang, S.Y.; Swennen, R.; Yang, T.; Yang, J.H.; Wu, N.Y.; Liu, J.A.; Chen, D.H. Chemical environment of cold seep carbonate formation on the northern continental slope of South China Sea: Evidence from trace and rare earth element geochemistry. *Mar. Geol.* **2010**, *277*, 21–30. [CrossRef]
64. Kim, J.H.; Torres, M.E.; Haley, B.A.; Kastner, M.; Pohlman, J.W.; Riedel, M.; Lee, Y.J. The effect of diagenesis and fluid migration on rare earth element distribution in pore fluids of the northern Cascadia accretionary margin. *Chem. Geol.* **2012**, *291*, 152–165. [CrossRef]
65. Prikryl, J.D.; Posey, H.H.; Kyle, J.R. A petrographic and geochemical model for the origin of calcite cap rock at Damon Mound Salt. *Chem. Geol.* **1988**, *74*, 67–97. [CrossRef]
66. Anderson, T.F.; Arthur, M.A. Stable isotopes of oxygen and carbon and their application to sedimentologic and paleoenvironmental problems. In *Stable Isotopes in Sedimentary Geology*; SEPM (Society for Sedimentary Geology): Dallas, TX, USA, 1983; pp. 1–151. [CrossRef]
67. Himmler, T.; Brinkmann, F.; Bohrmann, G.; Peckmann, J. Corrosion patterns of seep-carbonates from the eastern Mediterranean Sea. *Terra Nova* **2011**, *23*, 206–212. [CrossRef]
68. Feng, D.; Peckmann, J.; Li, N.; Kiel, S.; Qiu, J.W.; Liang, Q.; Carney, R.S.; Peng, Y.; Tao, J.; Chen, D. The stable isotope fingerprint of chemosymbiosis in the shell organic matrix of seep-dwelling bivalves. *Chem. Geol.* **2018**, *479*, 241–250. [CrossRef]
69. Guan, H.; Feng, D.; Birgel, D.; Peckmann, J.; Roberts, H.H.; Wu, N.; Chen, D. Lipid biomarker patterns reflect different formation environments of mussel- and tubeworm-dominated seep carbonates from the Gulf of Mexico (Atwater Valley and Green Canyon). *Chem. Geol.* **2019**, *505*, 36–47. [CrossRef]
70. Lepot, K.; Williford, K.H.; Philippot, P.; Thomazo, C.; Ushikubo, T.; Kitajima, K.; Mostefaoui, S.; Valley, J.W. Extreme ^{13}C-depletions and organic sulfur content argue for S-fueled anaerobic methane oxidation in 2.72 Ga old stromatolites. *Geochim. Cosmochim. Acta* **2019**, *244*, 522–547. [CrossRef]
71. Caesar, K.H.; Kyle, J.R.; Lyons, T.W.; Tripati, A.; Loyd, S.J. Carbonate formation in salt dome cap rocks by microbial anaerobic oxidation of methane. *Nat. Commun.* **2019**, *10*, 808. [CrossRef]

72. Aharon, P.; Graber, E.R.; Roberts, H.H. Dissolved carbon and $\delta^{13}C$ anomalies in the water column caused by hydrocarbon seeps on the northwestern Gulf of Mexico slope. *Geo-Mar. Lett.* **1992**, *12*, 33–40. [CrossRef]
73. Welch, S.E. Source(s) of Salinity in the Mississippi River Alluvial Aquifer, Iberville Parish, Louisiana. Master's Thesis, Louisiana State University, Baton Rouge, LA, USA, 2009.
74. Kennett, J.P.; Shackleton, N.J. Laurentide ice sheet meltwater recorded in Gulf of Mexico deep-sea cores. *Science* **1975**, *188*, 147–150. [CrossRef]
75. Palmer, M.R.; Edmond, J.M. The strontium isotope budget of the modern ocean. *Earth Planet. Sci. Lett.* **1989**, *92*, 11–26. [CrossRef]
76. Xu, Y.; Marcantonio, F. Strontium isotope variations in the lower Mississippi River and its estuarine mixing zone. *Mar. Chem.* **2007**, *105*, 118–128. [CrossRef]
77. McManus, K.M.; Hanor, J.S. Calcite and iron sulfide cementation of Miocene sediments flanking the West Hackberry salt dome, southwest Louisiana, U.S.A. *Chem. Geol.* **1988**, *74*, 99–112. [CrossRef]
78. Reilly, J.F., Jr.; MacDonald, I.R.; Biegert, E.K.; Brooks, J.M. Geologic controls on the distribution of chemosynthetic communities in the Gulf of Mexico. In *Hydrocarbon Migration and Its Near-Surface Expression. AAPG Memoir No. 66*; AAPG: Tulsa, OK, USA, 1996.
79. Lu, Y.; Liu, Y.; Sun, X.; Lin, Z.; Xu, L.; Lu, H.; Hao, X.; Peckmann, J. Intensity of methane seepage reflected by relative enrichment of heavy magnesium isotopes in authigenic carbonates: A case study from the South China Sea. *Deep Sea Res. Part I* **2017**, *129*, 10–21. [CrossRef]